

## ARTICLE

<https://doi.org/10.1038/s42005-019-0135-7>

OPEN

# Boosting magnetic resonance imaging signal-to-noise ratio using magnetic metamaterials

Guangwu Duan <sup>1</sup>, Xiaoguang Zhao<sup>1</sup>, Stephan William Anderson<sup>2</sup> & Xin Zhang <sup>1</sup>

Magnetic resonance imaging (MRI) represents a mainstay among the diagnostic imaging tools in modern healthcare. Signal-to-noise ratio (SNR) represents a fundamental performance metric of MRI, the improvement of which may be translated into increased image resolution or decreased scan time. Recently, efforts towards the application of metamaterials in MRI have reported improvements in SNR through their capacity to interact with electromagnetic radiation. While promising, the reported applications of metamaterials to MRI remain impractical and fail to realize the full potential of these unique materials. Here, we report the development of a magnetic metamaterial enabling a marked boost in radio frequency field strength, ultimately yielding a dramatic increase in the SNR (~ 4.2×) of MRI. The application of the reported magnetic metamaterials in MRI has the potential for rapid clinical translation, offering marked enhancements in SNR, image resolution, and scan efficiency, thereby leading to an evolution of this diagnostic tool.

<sup>1</sup>Department of Mechanical Engineering and Photonics Center, Boston University, Boston, MA 02215, USA. <sup>2</sup>Department of Radiology, Boston University Medical Campus, Boston, MA 02118, USA. These authors contributed equally: Guangwu Duan, Xiaoguang Zhao. Correspondence and requests for materials should be addressed to S.W.A. (email: [stephan.anderson@bmc.org](mailto:stephan.anderson@bmc.org)) or to X.Z. (email: [xinz@bu.edu](mailto:xinz@bu.edu))

Magnetic resonance imaging (MRI) represents a powerful diagnostic tool in the armamentarium of modern healthcare that is widely applied across a spectrum of diseases, from stroke to cancer imaging and beyond. When compared to alternative imaging modalities such as ultrasound or computed tomography, MRI offers the advantages of flexibility in generating image contrast from a range of tissue properties, leading to an inherently high degree of tissue contrast, as well as a lack of ionizing radiation. Chief among the performance metrics of MRI systems is the signal-to-noise ratio (SNR), which may be leveraged to boost overall acquisition performance, from image resolution to the efficiency of image acquisition, and has been demonstrated to improve anatomic delineation and detection of pathology<sup>1–5</sup>.

Over the past several decades, one of the fundamental methods by which to increase SNR in MRI has been through the development of platforms with increasingly powerful static magnetic fields (1.5 T, 3.0 T, and even 7.0 T clinical MRI systems). However, trade-offs of this approach are significant, including increases in hardware costs, image artifacts, patient side effects, tissue heating, and implanted hardware and medical device safety concerns<sup>6–9</sup>. In parallel, radiofrequency (RF) coil technology continues to improve and, currently, highly advanced multi-channel RF coils are routinely used in MRI<sup>10,11</sup>. In addition, a range of FDA-approved contrast agents, the majority of which are gadolinium-based, have been developed and are routinely employed in an effort to improve image quality and disease conspicuity. Finally, among other approaches, the ongoing design of sophisticated MRI pulse sequences and image-processing techniques yields further improvements in SNR, image quality, and overall scan efficiency<sup>12</sup>.

Beyond the aforementioned conventional and commonly employed techniques, metamaterials have been applied in an effort to enhance MRI capabilities. Metamaterials represent a class of artificially structured materials, which may be engineered in order to exhibit properties not found in naturally occurring materials. Importantly, the unique properties of metamaterials are derived not only from the inherent properties of their constituent materials but also from the precise arrangement of their internal structure, yielding powerful design flexibility. Typically, metamaterials feature a composition of elements (termed unit cells), the size and spacing of which are sufficiently small compared to the spatial variation of the exciting field. Since they were originally theoretically described and, more recently, experimentally validated, metamaterials have drawn interest due to their unique properties such as negative refraction index, among others<sup>13–15</sup>. With respect to MRI, the application of Swiss-roll and split-ring resonator arrays has been demonstrated to improve MRI coil sensitivity, yielding improvements in SNR<sup>16–18</sup>. Furthermore, magneto-inductive waveguides and flexible metamaterial endoscopes for MRI have also been reported to improve SNR and allow image transmission through a curved wire medium, respectively<sup>19,20</sup>. These early efforts at applying metamaterials to MRI, while promising, remain clinically impractical or, in some cases, superfluous or irrelevant to advancing modern MRI technology. More recently, a metasurface resonator has been reported to improve SNR in MRI using an ultrathin array of metallic wires<sup>21</sup>. However, limitations of this approach include magnetic field inhomogeneity and the potential for generating strong electric fields, raising potential safety concerns.

Here, we report the development of a magnetic metamaterial composed of an array of unit cells featuring metallic helices. While different schemes have been reported to manipulate and enhance magnetic fields, from static to radio frequencies<sup>22–26</sup>, we propose an array of metallic helical unit cells with collective resonant modes to interact with the magnetic field in MRI,

thereby improving SNR. Previously, we have reported the use of metallic helices in their application to wireless communication and charging in a sensor system, enabling a high degree of magnetic field confinement within the helices<sup>26</sup>, which is analogous to an electric field enhancement effect<sup>27,28</sup>. Relevant to the work reported herein is the fact that the magnetic field confinement also results in a marked degree of magnetic field enhancement in the vicinity of the helices. Therefore, by designing a metamaterial with unit cells composed of metallic helices, the metamaterial may inherit the capacity for field enhancement around a specific resonant mode. When applied to MRI, the resonant mode of the metamaterial may be excited by the radiofrequency (RF) magnetic fields employed during the MRI procedure, leading to a marked boost in RF field strength, ultimately leading to a dramatic increase in the SNR of MRI.

## Results

**Metamaterial structure design and analysis.** The magnetic metamaterial reported herein is comprised of an array of metallic helices (Fig. 1), the coupling of which leads to a synergy and bulk material property. The synergy of the metamaterial array yields the bulk property of a resonant mode in which the direction of the electric current induced by an applied RF field is identical in each unit cell. Upon excitation by an external RF field, the thusly-induced currents in the resonant mode lead to a dramatic enhancement of the RF field. With respect to MRI, when the frequency of the resonant mode approximates the resonance frequency of the MRI system, marked gains in both transmit and receive local RF magnetic fields ( $B_1+$  and  $B_1-$ , respectively) are achieved, ultimately leading to gains in SNR.

In order to elucidate the determinants of the resonant mode of the metamaterial, electromagnetic theory can firstly be employed to define the equivalent self-inductance and mutual inductance of discrete unit cells as<sup>29</sup>:

$$L_{ij} = \frac{\mu_0}{4\pi|I_i I_j|} \iint dr_i dr_j \frac{J(r_i) \cdot J(r_j)}{|r_i - r_j|}, \quad (1)$$

where  $r_i$  and  $r_j$  are the integration elements along the path of the helix,  $I_i$  and  $I_j$  are the equivalent current in the helix, and  $J(r_i)$  and  $J(r_j)$  are the current densities (vectors) at  $r_i$  and  $r_j$ . Eq. 1 represents the self-inductance when  $i$  is equal to  $j$  and mutual inductance when  $i$  and  $j$  are different. At the resonant state, the amplitude of the current follows a sinusoidal profile along the path of the

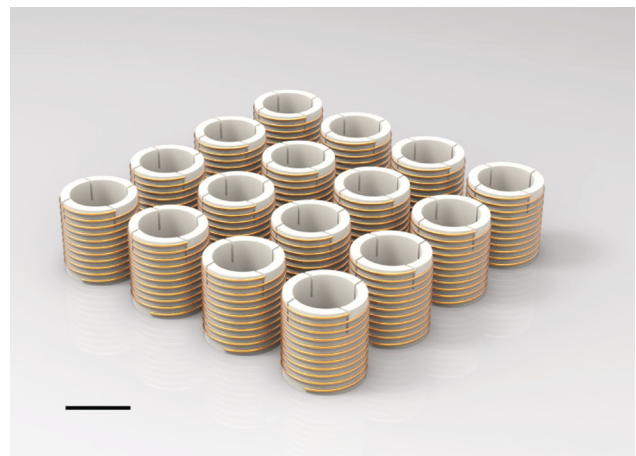


**Fig. 1** Schematic of the magnetic metamaterial. The metamaterial array composes unit cells featuring metallic helices, which are made of copper wiring with central polymeric scaffolding. Scale bar is 3 cm. (Dimensions included for scale and employed in subsequent analyses, see Methods)

wire of the helix with a maximum ( $I_0$ ) at the center and zero at the ends of the wire<sup>29</sup>. Thusly,  $I_{ij} = I_0/\sqrt{2}$ . The self-capacitance and mutual capacitance can be calculated by finding the inverse of the coefficients of the potential matrix<sup>30</sup> and, by employing electromagnetic theory, be expressed as:

$$P_{ij} = \frac{1}{4\epsilon_0\epsilon_r|Q_iQ_j|} \iint dr_i dr_j \frac{\rho(r_i)\rho(r_j)}{|r_i - r_j|}. \quad (2)$$

$$\begin{bmatrix} C_{11} & \cdots & C_{1m} \\ \vdots & \ddots & \vdots \\ C_{m1} & \cdots & C_{mm} \end{bmatrix} = \begin{bmatrix} P_{11} & \cdots & P_{1m} \\ \vdots & \ddots & \vdots \\ P_{m1} & \cdots & P_{mm} \end{bmatrix}^{-1}, \quad (3)$$

in which  $Q_i$  and  $Q_j$  are the equivalent charge amounts in the helix and  $\rho(r_i)$  and  $\rho(r_j)$  are the charge densities (scalars) at  $r_i$  and  $r_j$ . The phase difference between the current and charge distribution is  $\pi/2$  and, therefore, the maximal charge density is at the two ends of the helical wire ( $q_0$ ) and zero at the middle of the wire. Taking into consideration the charge distribution,  $Q_{ij} = q_0 l_i \pi / \sqrt{2}$  where  $l_i$  is the total length of the wire wound to

form the helix. The diagonal elements of the capacitance matrix yield the self-capacitance, while the remaining elements yield the corresponding mutual capacitance.

Upon implementation of the discrete unit cells into a metamaterial array, the effect of coupling must be considered, given its ultimate effect upon the resonant mode of the array. As the geometry of each unit cell is identical, the coupling coefficient of two adjacent helices may be expressed as  $k = C_m/C + L_m/L$ , in which  $C_m$  and  $L_m$  represent the mutual capacitance and mutual inductance, respectively, and  $C$  and  $L$  represent the self-capacitance and self-inductance, respectively. The total coupling coefficient ( $k$ ), as well as the contributions from capacitance coupling ( $k_c$ ) and inductance coupling ( $k_l$ ) are plotted as a function of unit cell separation distance in Fig. 2.  $k_c$  and  $k_l$  are both negative and  $k_c$  is approximately 3-fold larger than  $k_l$ , demonstrating that a much larger contribution to the total coupling stems from the capacitance coupling between unit cells. In order to validate these theoretical results, numerical analyses were also conducted to derive the coupling coefficient and plotted in Fig. 2 (please see Supplementary Note 1 for further details).

Finally, due to the coupling between the discrete unit cells of the array, the resonant modes of the metamaterial may be derived by employing the coupled mode theory and solving the following equation system<sup>31,32</sup>:

$$\frac{da_n(t)}{dt} = -(j\omega_0 + \Gamma_n)a_n(t) + j \sum_{k=1}^{m, k \neq n} K_{kn} a_k(t), \quad n = 1, \dots, m, \quad (4)$$

in which  $\omega_0 = 1/\sqrt{LC}$  represents the resonant angular frequency of a single helix,  $\Gamma_n$  is the intrinsic decay introduced by the material and radiation losses,  $K_{kn}$  is the coupling factor among unit cells and is related to the coupling coefficient  $k$  as  $K_{kn} = k\omega_0/2$ , and  $m$  is the total number of unit cells. The loss of each unit cell is omitted and only the coupling between adjacent unit cells is considered for simplicity to derive the resonant modes of the metamaterial (please see Supplementary Note 2 for further details). The eigenvalue represents the resonant frequency of the resonant mode and the corresponding eigenvector indicates the resonant strength and direction of each unit cell of the mode. By analyzing the resultant matrix, one can identify that the current direction in each unit cell is identical for the resonant mode with the highest resonant frequency, which will be referred to as the working mode.

The working mode of a metamaterial ordered as a  $4 \times 4$  array as a function of unit cell separation distance was calculated, compared with simulation results, and illustrated in Fig. 3a.

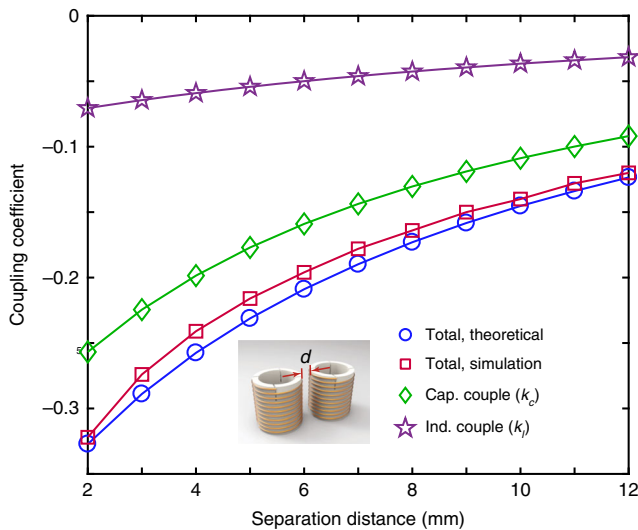


**Fig. 2** Coupling coefficients between adjacent unit cells. Coupling coefficients as a function of unit cell separation distance derived from both theoretical and numerical analyses

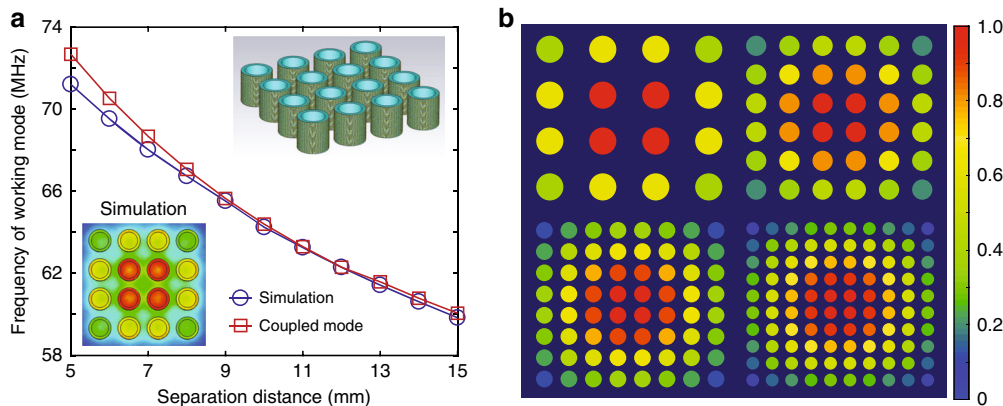


**Fig. 3** Resonant mode of the metamaterials. **a** The frequency of the working mode of the metamaterial as a function of separation distance of unit cells. Inset on the bottom left plots the simulated magnetic field at the middle cross-section of the metamaterials. Inset on the top right depicts the model used for simulation. **b** The resonant strength derived from the coupled mode theory for metamaterials with  $4 \times 4$ ,  $6 \times 6$ ,  $8 \times 8$ , and  $10 \times 10$  arrays. The resonant strength is normalized to the maximum value

The degree of difference between the simulation results and the coupled mode theory increases as the coupling increases with decreasing separation distance, which is due to the weak coupling assumption of the coupled mode theory. However, as the separation distance increases, the theoretical results demonstrate a high degree of agreement with the simulation results. The working modes for metamaterials composed of different numbers of unit cells are also illustrated in Fig. 3b with identical spacing between unit cells. The colors correspond to the resonant strength of each unit cell derived from the coupled mode theory. The unit cells at the center are found to resonate with the greatest strength, while the resonant strength decreases for the unit cells positioned along the periphery, thereby leading to larger degrees of magnetic field enhancement at the center of the metamaterials. For purposes of comparison, the relative magnetic field strength at the middle cross-section of a  $4 \times 4$  metamaterial array is also simulated in CST Studio Suite 2017 and plotted as the inset at the bottom left corner in Fig. 3a, demonstrating a similar resonant strength pattern to that derived from the coupled mode theory.

**Magnetic field distribution and field enhancement.** Upon deployment of the metamaterials inside the bore of an MRI, by matching the frequency of the working mode to the working frequency of the MRI, the working mode can be excited by the RF magnetic field generated by the MRI (both transmit and receive RF magnetic fields;  $B_{1+}$  and  $B_{1-}$ , respectively). The RF magnetic field leads to the induction of an AC voltage across the helix as  $V = nS (dB_{1+})/dt$ . The impedance of the helix can be expressed as  $Z_i = j\omega L + 1/j\omega C + R$ , where  $L$  and  $C$  are the equivalent inductance and capacitance of the unit cell in the array, respectively, and  $R$  is the equivalent resistance, which is composed of the ohmic loss of the wire, as well as the dielectric loss of the scaffolding material. Therefore, the current inside the metallic helix can be calculated by  $I = V/Z_i$ . The induced magnetic field contains two components, along the axial direction and the radial direction. Only the magnetic field component along the axial direction of the helix contributes to the magnetic field enhancement and can be calculated as<sup>33</sup>:

$$B_z = \frac{\mu_0 n I_0 a}{4\pi l} \int_{-l/2}^{l/2} \cos\left(\frac{\pi z'}{l}\right) \int_0^{2\pi} \frac{a - \rho \cos(\varphi')}{[\rho^2 - 2a\rho \cos(\varphi') + a^2 + (z - z')^2]^{3/2}} d\varphi' dz', \quad (5)$$

in which  $I_0$  is the amplitude of the current at the middle of the helix,  $n$  is the number of turns of the helix,  $a$  is the radius of the helix,  $l$  is the height of the helix,  $\rho$  and  $z$  are the polar coordinates of the target point, and  $\cos(\pi z'/l)$  reflects the current distribution along the helix (please see Supplementary Note 3 for further details). The magnetic field enhancement ratio can be calculated by the summation of the magnetic field components (including the magnetic field generated by each unit cell and  $B_{1+}$ ) and normalizing to  $B_{1+}$ , with the current strength in each unit cell indicated by the eigenvector of the coupled mode theory.

The magnetic field enhancement ratio at the mid-portion of the metamaterials along the axial direction is calculated and plotted as a function of distance from the metamaterial array in Fig. 4a. The magnetic field enhancement analysis is divided into three regions. Region A (shaded orange in Fig. 4a) is within the metamaterial and, although extremely high magnetic field enhancement is realized, this region is impractical for application to MRI imaging, as is considered herein. Region B (shaded yellow in Fig. 4a) extends from surface of the metamaterial to a distance where the direction of the magnetic field changes to the same direction as  $B_{1+}$  and the peak enhancement ratio outside the metamaterial is realized. Region C begins at and extends beyond the peak enhancement ratio distance and may be considered the optimal region for placement of a sample to be imaged in MRI ('sample region'). The inset illustrates an extended analysis of the enhancement ratio of the sample region (Region C), indicating maximum magnetic field enhancement ratios of 5.84 and 6.01 for calculation and simulation results, respectively. Figure 4b depicts the simulated magnetic field distribution at the highlighted cross-section of the inset. The field enhancement ratio along the white dashed line is plotted in Fig. 4a, demonstrating a high degree of agreement with the theoretical results. In addition to the decay of the magnetic field enhancement, the direction of the magnetic field in the vicinity of the metamaterials also varies at different locations, as shown in the Supplementary Fig. 3. The magnetic field strength decay and direction variation lead to the gradient in the SNR enhancement.

Finally, the magnetic field enhancement ratios of metamaterials composed of unit cells with different diameters were also theoretically modeled. As plotted in Fig. 4c, with the increase in the diameter, the peak enhancement ratio decreases accordingly and exhibits a relatively slower decay rate as a function of distance from the metamaterial array.

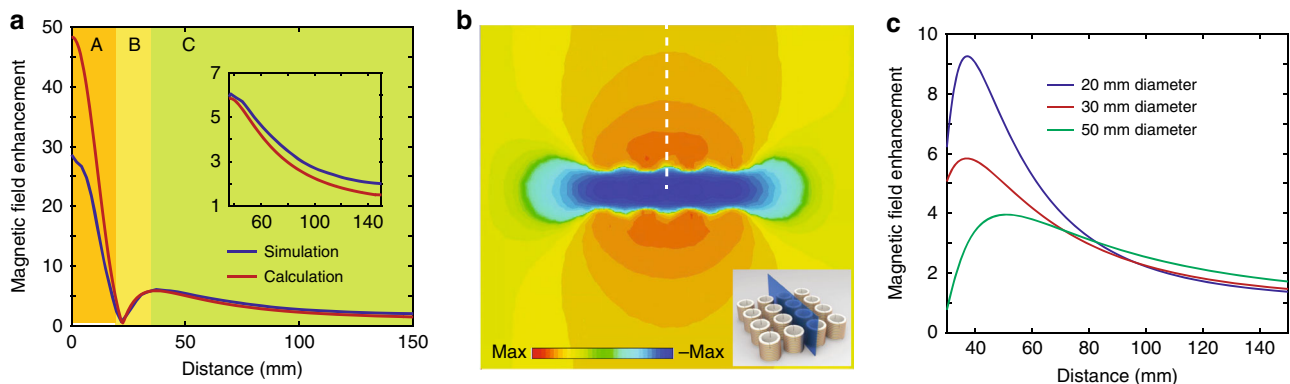


**Fig. 4** Magnetic field enhancement ratio of the metamaterials. **a** Magnetic field enhancement ratio as a function of distance from the center of the metamaterial array (along the white dashed line in **b**) with simulation and calculation results in blue and red. Regions A, B, and C correspond to the regions within the metamaterial array, the region extending from the surface of the metamaterial to the peak enhancement ratio, and the 'sample region' beyond the peak enhancement, respectively. The inset illustrates an extended plot of Region C ('sample region'). **b** The magnetic field strength along the axial direction distributed at the cross-section depicted as the blue rectangle in the inset. **c** The theoretical magnetic field enhancement ratio of metamaterials with unit cells with different diameters

**Noise analysis and SNR improvement.** The expression for SNR in MRI, originally formulated by Hoult and Lauterbur<sup>34,35</sup>, is:

$$\text{SNR} \propto \frac{\omega^2 B_c}{\sqrt{r_{\text{coil}} + r_{\text{sample}}}}, \quad (6)$$

where  $B_c$  is the magnetic field strength generated with unit current in the receiving coil and  $r_{\text{coil}}$  is the resistance of the receiving coil.  $r_{\text{sample}}$  is the equivalent resistance of the sample in the receiving coil, which can generate the same amount of heat with unit current as the heat generated by the induced current in the sample by the RF magnetic field<sup>36,37</sup>, as detailed in Supplementary Note 4. Through the application of the magnetic metamaterial,  $B_c$  may be enhanced due to the RF magnetic field enhancement detailed above, thereby increasing the signal. However, the introduction of the metamaterial also leads to an increase in the noise by increasing the total power dissipation, with a nearly 1.5-fold increase in the noise derived for our design (please see Supplementary Note 5 for further details).

If  $B_c$  is constant and  $r_{\text{sample}}$  is much larger than  $r_{\text{coil}}$ , the substitution of Eq. S18 in Supplementary Note 5 into Eq. 6 would seem to indicate that both signal and noise scale to an identical degree, thereby resulting in an absence of a net gain in SNR. Importantly, however, the introduction of the metamaterial results in the generation of a magnetic field gradient (see Fig. 4a). Therefore, as the degree of RF magnetic field enhancement along the sample in proximity to the metamaterial exceeds the increase in noise, significant gains in SNR are realized in Region C of Fig. 4a. Also notable is the capacity to tune the RF magnetic field enhancement gradients of the metamaterial through precise array design (such as unit cells with different diameters, see Fig. 4c), enabling the tailored application of metamaterials in MRI as a function of the tissue depth of interest, which is demonstrated below. Furthermore, it is noted that  $r_{\text{sample}}$  is proportional to the 4th order of the radius of the sample (please see Supplementary Note 5 for further details). Thus, when imaging small parts (knees, wrists, etc.),  $r_{\text{coil}}$  dominates the noise and the degree of RF magnetic field enhancement approximates the ultimate gains in SNR. The effect of the metamaterial on the electric field in MRI has also been investigated, demonstrating that the metamaterial has little effect on the electric field in the region of interest, thereby avoiding an increase in specific absorption rate (SAR) resulted from the application of the metamaterial during the imaging process (please see Supplementary Note 6 for further details).

**Experimental MRI validation.** Helices with identical geometries to the theoretical models employed in the analyses above were fabricated and employed for subsequent experimental validation. We employed 3D printing to fabricate hollow cylinders with grooves along their outer surface to serve as scaffolding (ABS P430). Subsequently, copper wires were wound along the 3D printed grooves in order to form the helices. Finally, the individual unit cells were aligned in an array in order to construct the complete magnetic metamaterial. Metamaterial arrays of two distinct geometries ( $4 \times 4$  array with unit cell diameter of 3 cm,  $3 \times 3$  arrays with unit cell diameter of 5 cm) were fabricated and designed with a resonance frequency of 63.8 MHz, the operating frequency of the 1.5 T MRI employed herein. The two geometries of the metamaterials served to experimentally illustrate the capacity for tuning the RF magnetic field enhancement gradients (see Fig. 4c) such that the degree of SNR enhancement imaging may be optimized for more superficial (spine, for example) or deeper structures (liver, for example).

MRI experiments were performed in a clinical 1.5 T MRI and the birdcage body RF coil, located within the bore of the MRI

system, was used for both RF transmission and reception ( $B_{1+}$  and  $B_{1-}$ , respectively). The resonant frequency detuning of the body RF coil due to the presence of the metamaterials is trivial based on our simulation (from 64.14 to 64.62 MHz) and may be readily compensated by the MRI system. Phantom MRI samples were prepared for imaging and composed of 2% agar gel in a 3D printed cubic mold with side length of 10 cm. Gradient echo imaging was performed both with and without the presence of the two distinct metamaterial arrays placed along the undersurface of the phantoms (top surface of the metamaterial array placed 2 cm from the bottom surface of the agar phantom; see Fig. 5a) (please see Methods for further details regarding MRI experiments). Given that the metamaterials led to enhancement of both transmission and reception RF energy (5.84 as shown in Fig. 4a), the transmission RF energy during the metamaterial-enhanced experiments was decreased such that, upon enhancement of  $B_{1+}$ , would approximate the transmission RF energy of control experiments employed for comparison of SNR. MRI images of the phantom with and without the presence of the  $4 \times 4$  metamaterial array with unit cell diameter of 3 cm are shown in Fig. 5b, c, respectively, demonstrating a 4.2-fold increase in SNR. In addition, the degree of SNR enhancement achieved experimentally is compared to simulation and theoretical results in Fig. 5d, demonstrating a high degree of agreement.

Subsequently, a similar experimental approach was also conducted with metamaterials featuring a unit cell diameter of 5 cm in a  $3 \times 3$  array. The MRI image in the presence of this metamaterial array is shown in Fig. 6a and a comparison of the experimental SNR enhancement ratios of the two distinct array geometries is shown in Fig. 6b. Notably, a lower peak SNR enhancement and slower decay rate as a function of distance from the metamaterial array are demonstrated with the larger unit cell diameter, similar to Fig. 4c.

Finally, MRI experiments were performed using a chicken leg to demonstrate the SNR enhancement capabilities of the magnetic metamaterial arrays. The experimental setup depicted in Fig. 5a was employed, along with identical MRI pulse sequences, but having replaced the phantom with a chicken leg. Images were acquired in the plane parallel to the top surface of the metamaterial array at distances of 2.25 cm (for Fig. 7a, b) and 2.50 cm (for Fig. 7c, d) from the array. In this case, when compared to images acquired in the absence of the metamaterial array (Fig. 7b, d), SNR enhancement of up to 3.6-fold was achieved (Fig. 7a, c) in the presence of the metamaterial. As a point of further consideration, currently, an alternative approach to increasing SNR commonly employed in clinical MRI is the use of signal averaging. In this case, all other experimental conditions remaining fixed, a 13.9-fold increase in scan time would be required to achieve a similar increase without the presented metamaterial in SNR through signal averaging, highlighting the potential utility of metamaterial-enhanced MRI.

## Discussion

We have developed a magnetic metamaterial which, in its application to MRI, serves to enhance the RF magnetic fields and increase SNR. While the experimental validation reported herein was carried out using the body RF coil, the metamaterial may be readily employed in combination with surface RF receive coils. Alternatively, the combination of magnetic metamaterials with a body RF coil employed for both transmission and reception may be an avenue towards decreasing the technical complexity and cost of optimal surface RF receive coils. To enhance the practicality of this approach, future efforts may be directed at achieving a 'smart' metamaterial operating only during the RF reception phase of the MRI experiment. In this fashion, through either

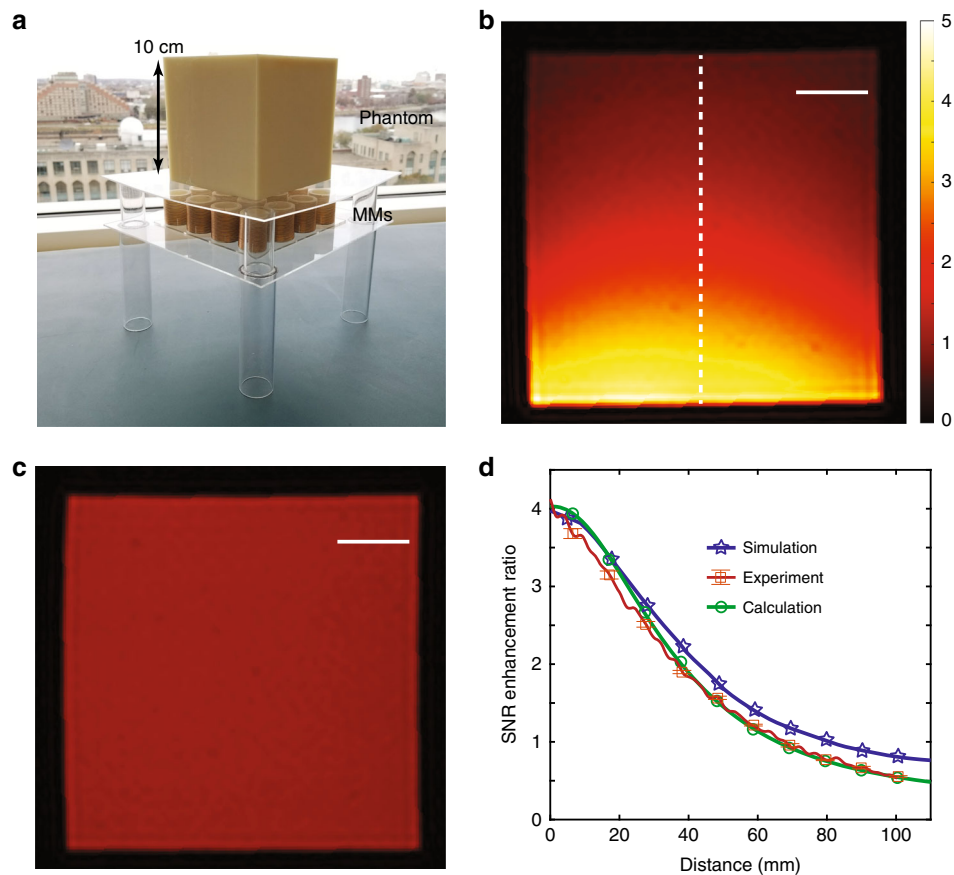


**Fig. 5** Experimental results with and without metamaterials. **a** Experimental setup of metamaterial array beneath 3D printed magnetic resonance imaging (MRI) phantom containing 2% agar gel. **b** MRI image in presence of  $4 \times 4$  metamaterial array with unit cell diameter of 3 cm (transmission radio frequency (RF) power of MRI experiment reduced, see Methods; the dashed line used for comparison of signal-to-noise ratio (SNR) in **d**). **c** Control MRI image in the absence of metamaterial array (transmission RF energy not reduced, see Methods). Scale bars correspond to 2 cm in **b**, **c**. **d** Comparison of SNR enhancement ratios of experimental, simulation, and calculation results. The bars for experimental results show the standard deviation of the measured SNR enhancement ratio

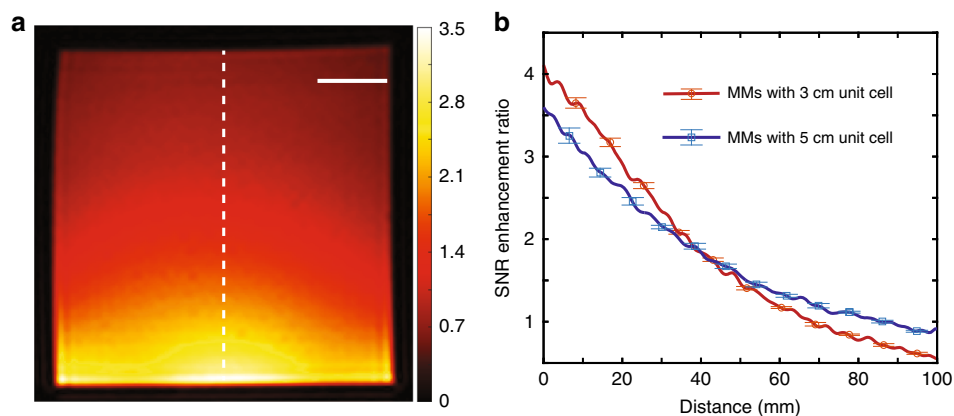


**Fig. 6** Experimental results with larger unit cells. **a** Magnetic resonance imaging (MRI) image in presence of  $3 \times 3$  metamaterial array with a diameter of 5 cm (transmission radio frequency (RF) power of MRI experiment reduced, see Methods; the dashed line used for comparison of signal-to-noise ratio (SNR) in **b**). The scale bar is 2 cm. **b** Comparison of SNR enhancement ratios of metamaterial arrays with distinct unit cell diameters. The larger unit cell (blue line) exhibits lower peak SNR enhancement and slower decay rate as a function of distance from the top surface of the metamaterial array. The bars for experimental results show the standard deviation of the measured SNR enhancement ratio

active or passive switching approaches, the metamaterial may be employed without any unwanted modifications to the MRI pulse sequences or safety concerns related to inappropriate RF energy deposition (maintaining SAR within specified standard levels). Furthermore, optimization of the materials choices and array

design may further improve the performance of the magnetic metamaterials, such as employing low-loss material and/or optimizing the configuration of the metamaterials to further increase the SNR boost. Finally, the physical footprint of the metamaterials may be significantly reduced through the use of high

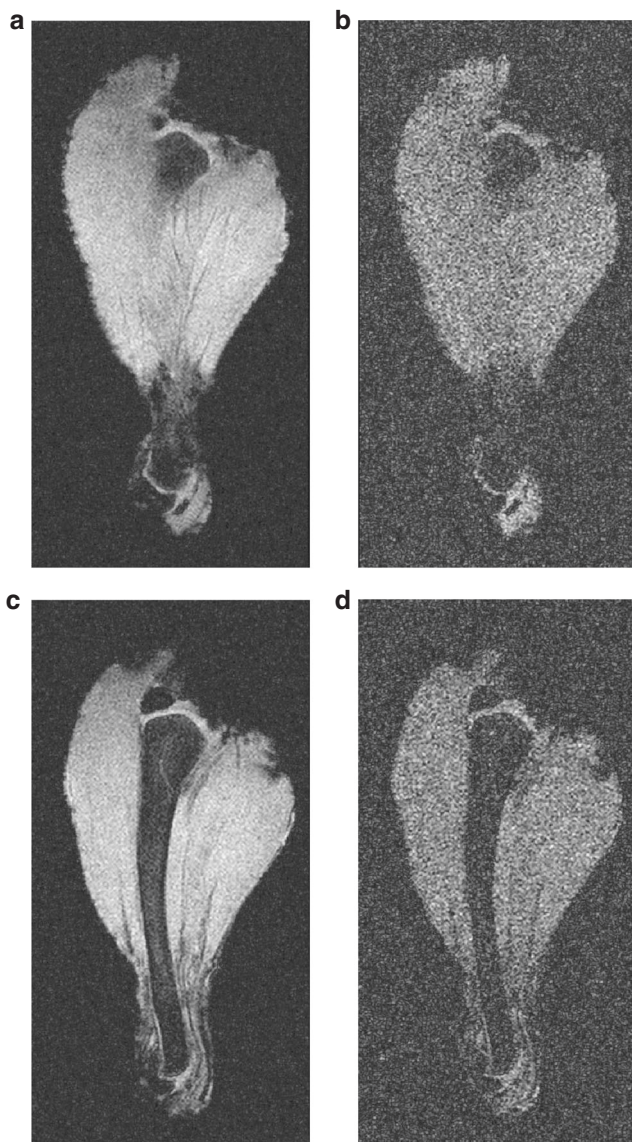


**Fig. 7** MRI scan of a chicken leg. Images acquired 2.25 cm (**a, b**) and 2.50 cm (**c, d**), from the top surface of the metamaterial array. Images (**a, c**) are acquired in the presence of the metamaterial array while images (**b, d**) are acquired in the absence of the metamaterial array. All other experimental conditions remain fixed between scans

permittivity, low-loss scaffolding materials, and insulating wire coatings, thereby allowing for flexible, sheet-like materials that may be readily used in combination or directly integrated with surface RF coils. While the focus of this work was on increasing SNR, an alternative consideration in its application to MRI would be to focus on the utility of the enhancement of the transmission RF energy that, for example, may lead to lower RF power amplifier hardware requirements. In summary, we report the development of magnetic metamaterials and validate their application to MRI in order to improve the SNR, a fundamental performance metric that may be leveraged to drive improvements in the overall acquisition quality, from image resolution to the efficiency of image acquisition.

## Methods

**Geometry of the metamaterial structure.** A  $4 \times 4$  metamaterial array, as shown in Fig. 1, was employed to conduct the theoretical analyses. The geometries of each helix were 32, 15, 0.28 mm, and 25 for height, radius, wire diameter and number

of turns, respectively. The wires of the helices were composed of copper and the permittivity of the scaffolding core material was assumed as  $2 \times (1 + 0.03j)$  (ABS P430). An additional  $3 \times 3$  arrays were employed during the MRI experiments in order to demonstrate the manipulation of the field enhancement gradient and featured geometries of 30, 25, 0.28 mm, and 12 for height, radius, wire diameter and number of turns, respectively. The resonant frequencies of the metamaterial were tuned and measured with a network analyzer by utilizing a coupling loop in order to match the working frequency of a 1.5 T MRI at 63.8 MHz.

**Magnetic resonance imaging validation.** All MRI experiments were performed in a 1.5 T clinical MRI system (Intera, Philips Healthcare). A gradient echo pulse sequence (TE = 13.81 ms, TR = 1600 ms) was employed throughout. Given that the metamaterials lead to an enhancement of transmission RF energy, the transmission energy was reduced during the MRI experiments in the presence of the metamaterial array. To this end, the flip angle of the gradient echo image acquisition was decreased to  $18^\circ$ , given the expected transmission RF energy increase of  $\sim 5$ -fold (see Fig. 4). In the absence of the metamaterial arrays, a  $90^\circ$  flip angle was employed, allowing for a comparison of MRI SNR with and without the presence of the metamaterials while mitigating the confounding effect of RF transmission energy enhancement.

**Reporting Summary.** Further information on experimental design is available in the Nature Research Reporting Summary linked to this article.

## Data availability

All data needed to support the conclusions in the paper and the Supplementary Information are available from the corresponding authors upon reasonable request.

Received: 1 November 2018 Accepted: 21 February 2019

Published online: 26 March 2019

## References

- Owen, R. S. & Wehrli, F. W. Predictability of SNR and reader preference in clinical MR imaging. *Magn. Reson. Imaging* **8**, 737–745 (1990).
- Kuhl, C. K. et al. Acute and subacute ischemic stroke at high-field-strength (3.0-T) diffusion-weighted MR imaging: intraindividual comparative study. *Radiology* **234**, 509–516 (2005).
- Fischbach, F., Muller, M. & Bruhn, H. Magnetic resonance imaging of the cranial nerves in the posterior fossa: a comparative study of t2-weighted spin-echo sequences at 1.5 and 3.0 tesla. *Acta Radiol.* **49**, 358–363 (2008).
- Fischbach, F. et al. Magnetic resonance imaging of hyaline cartilage defects at 1.5T and 3.0T: comparison of medium T2-weighted fast spin echo, T1-weighted two-dimensional and three-dimensional gradient echo pulse sequences. *Acta Radiol.* **46**, 67–73 (2005).
- Michaely, H. J. et al. Intraindividual comparison of high-spatial-resolution abdominal MR angiography at 1.5T and 3.0T: Initial experience. *Radiology* **244**, 907–913 (2007).
- Stahl, R. et al. Assessment of cartilage-dedicated sequences at ultra-high-field MRI: comparison of imaging performance and diagnostic confidence between 3.0 and 7.0 T with respect to osteoarthritis-induced changes at the knee joint. *Skelet. Radiol.* **38**, 771–783 (2009).
- Mazaheri, Y. et al. Image artifacts on prostate diffusion-weighted magnetic resonance imaging: trade-offs at 1.5 Tesla and 3.0 Tesla. *Acad. Radiol.* **20**, 1041–1047 (2013).
- Versluis, M. J. et al. Subject tolerance of 7 T MRI examinations. *J. Magn. Reson. Imaging* **38**, 722–725 (2013).
- Kollia, K. et al. First clinical study on ultra-high-field MR imaging in patients with multiple sclerosis: comparison of 1.5T and 7T. *AJNR Am. J. Neuroradiol.* **30**, 699–702 (2009).
- Porter, J. R., Wright, S. M. & Reykowski, A. A 16-element phased-array head coil. *Magn. Reson. Med.* **40**, 272–279 (1998).
- Sengupta, S. et al. A specialized multi-transmit head coil for high resolution fMRI of the human visual cortex at 7T. *PLoS. One.* **11**, e0165418 (2016).
- Lustig, M., Donoho, D. & Pauly, J. M. Sparse MRI: The application of compressed sensing for rapid MR imaging. *Magn. Reson. Med.* **58**, 1182–1195 (2007).
- Veselago, V. G. The electrodynamics of substances with simultaneously negative values of  $\epsilon$  and  $\mu$ . *Sov. Phys. Uspekhi* **10**, 509–518 (1968).
- Pendry, J. B. et al. Magnetism from conductors and enhanced nonlinear phenomena. *IEEE Trans. Microw. Theory Techn.* **47**, 2075–2084 (1999).
- Shelby, R. A., Smith, D. R. & Schultz, S. Experimental verification of a negative index of refraction. *Science* **292**, 77–79 (2001).
- Wiltshire, M. C. et al. Microstructured magnetic materials for RF flux guides in magnetic resonance imaging. *Science* **291**, 849–851 (2001).

17. Freire, M. J., Marques, R. & Jelinek, L. Experimental demonstration of a  $\mu = -1$  metamaterial lens for magnetic resonance imaging. *Appl. Phys. Lett.* **93**, 231108 (2008).
18. Freire, M. J., Jelinek, L., Marques, R. & Lapine, M. On the applications of  $\mu = -1$  metamaterial lenses for magnetic resonance imaging. *J. Magn. Reson.* **203**, 81–90 (2010).
19. Syms, R. R. A., Floume, T., Young, I. R., Solymar, L. & Reab, M. Flexible magnetoinductive ring MRI detector: Design for invariant nearest-neighbour coupling. *Metamaterials* **4**, 1–14 (2010).
20. Radua, X., Garayb, D. & Craeyea, C. Toward a wire medium endoscope for MRI imaging. *Metamaterials* **3**, 90–99 (2009).
21. Slobozhanyuk, A. P. et al. Enhancement of magnetic resonance imaging with metasurfaces. *Adv. Mater.* **28**, 1832–1838 (2016).
22. Oh, J. et al. Detection of magnetic nanoparticles in tissue using magneto-motive ultrasound. *Nanotechnology* **17**, 4183–4190 (2006).
23. Park, J.-K. et al. 3D field phase-space control in tokamak plasmas. *Nat. Phys.* **14**, 1223–1228 (2018).
24. Chabalko, M. J., Besnoff, J. & Ricketts, D. S. Magnetic field enhancement in wireless power with metamaterials and magnetic resonant couplers. *IEEE Antennas Wirel. Propag. Lett.* **15**, 452–455 (2016).
25. Sun, J. et al. Experimental demonstration of anomalous field enhancement in all-dielectric transition magnetic metamaterials. *Sci. Rep.* **5**, 16154 (2015).
26. Duan, G., Zhao, X. & Zhang, X. A magnetically coupled communication and charging platform for microsensors. *J. Micro. Syst.* **26**, 1099–1109 (2017).
27. Valagiannopoulos, C. A. & Sihvola, A. Improving the electrostatic field concentration in a negative-permittivity wedge with a grounded “bowtie” configuration. *Radio Sci.* **48**, 316–325 (2013).
28. Bionta, M. R. et al. Wavelength and shape dependent strong-field photoemission from silver nanotip. *New J. Phys.* **18**, 103010 (2016).
29. Kurs, A. et al. Wireless power transfer via strongly coupled magnetic resonances. *Science* **317**, 83–86 (2007).
30. Huray, P. G. *Maxwell's Equation*. (John Wiley & Sons, New Jersey, 2010).
31. Haus, H. A. *Waves and Fields in Optoelectronics*. (Prentice-Hall, New Jersey, 1984).
32. Karalis, A., Joannopoulos, J. D. & Soljacic, M. Efficient wireless non-radiative mid-range energy transfer. *Ann. Phys.* **323**, 34–48 (2008).
33. Derby, N. & Olbert, S. Cylindrical magnets and ideal solenoids. *Am. J. Phys.* **78**, 229–235 (2010).
34. Hayes, C. E. & Axel, L. Noise performance of surface coils for magnetic resonance imaging at 1.5T. *Med. Phys.* **12**, 604–607 (1985).
35. Hoult, D. I. & Richards, R. E. The signal-to-noise ratio of the nuclear magnetic resonance experiment. *J. Magn. Reson.* **24**, 71–85 (1976).
36. Hong, J. S. & Lancaster, M. J. *Microstrip Filters for RF/microwave Applications*. (John Wiley & Sons, New Jersey, 2001).
37. Hoult, D. I. The sensitivity of the Zeugmatographic experiment involving human samples. *J. Magn. Reson.* **34**, 425–433 (1979).

## Acknowledgements

This research was supported by the National Institute of Health (NIH) of Biomedical Imaging and Bioengineering grant 1R21EB024673. This research was also supported by the Boston University College of Engineering Dean's Catalyst Award and the Boston University Wallace H. Coulter Translational Research Partnership Award. We thank the Boston University Photonics Center for technical support. We are thankful to Ning Hua, Mitchell Horn, and Zhikuan Zhu for their experimental assistance during the MRI testing and Thomas Bifano and Hernan Jara for helpful discussions.

## Author contributions

X. Zhang and S.W.A. conceived the study. G.D., X. Zhao and X. Zhang conducted the numerical modeling and theoretical analysis, G.D., X. Zhao and X. Zhang constructed the metamaterials. All authors performed experiments, analyzed data and wrote the manuscript.

## Additional information

**Supplementary information** accompanies this paper at <https://doi.org/10.1038/s42005-019-0135-7>.

**Competing interests:** We have filed a patent application on the work described herein. Applicant: Trustees of Boston University. Inventors: Xin Zhang, Stephan Anderson, Guangwu Duan, and Xiaoguang Zhao. Application Number: 16/002,458. Status: Pending.

**Reprints and permission** information is available online at <http://npg.nature.com/reprintsandpermissions/>

**Publisher's note:** Springer Nature remains neutral with regard to jurisdictional claims in published maps and institutional affiliations.



**Open Access** This article is licensed under a Creative Commons Attribution 4.0 International License, which permits use, sharing, adaptation, distribution and reproduction in any medium or format, as long as you give appropriate credit to the original author(s) and the source, provide a link to the Creative Commons license, and indicate if changes were made. The images or other third party material in this article are included in the article's Creative Commons license, unless indicated otherwise in a credit line to the material. If material is not included in the article's Creative Commons license and your intended use is not permitted by statutory regulation or exceeds the permitted use, you will need to obtain permission directly from the copyright holder. To view a copy of this license, visit <http://creativecommons.org/licenses/by/4.0/>.

© The Author(s) 2019